

Appendix

A Calculation of forward responses in REBOCC

A.1 Solution of the induction problem

In two-dimensional structures, the physical process of electromagnetic induction is described by two separate equations for the two polarizations (time dependency: $e^{-i\omega t}$):

$$\nabla \times \nabla \times \mathbf{E} = i\omega\mu_0\sigma\mathbf{E} \quad \text{TE-mode} \quad (\text{A.1a})$$

$$\nabla \times \rho\nabla \times \mathbf{H} = i\omega\mu_0\mathbf{H} \quad \text{TM-mode} \quad (\text{A.1b})$$

Within REBOCC, these equations are solved with the method of finite-difference approximations (FD) for models of discrete rectangular blocks of homogenous isotropic conductivity. Discretization of the problem is as in *Smith and Booker [1991]* (see also *Apra et al. [1997]*) and partly described below. Since this study concentrates on magnetic fields, only the TE-mode is treated.

Let x be the direction of the structural strike. Then the equation to be solved is:

$$\begin{aligned} (\nabla \times \nabla \times \mathbf{E})_x &= (\nabla \cdot \nabla \mathbf{E})_x - (\Delta \mathbf{E})_x \\ &= -\nabla \cdot \nabla E_x = -\Delta E_x = -\left(\frac{\partial^2 E_x}{\partial y^2} + \frac{\partial^2 E_x}{\partial z^2}\right) = i\omega\mu_0\sigma E_x \end{aligned} \quad (\text{A.2})$$

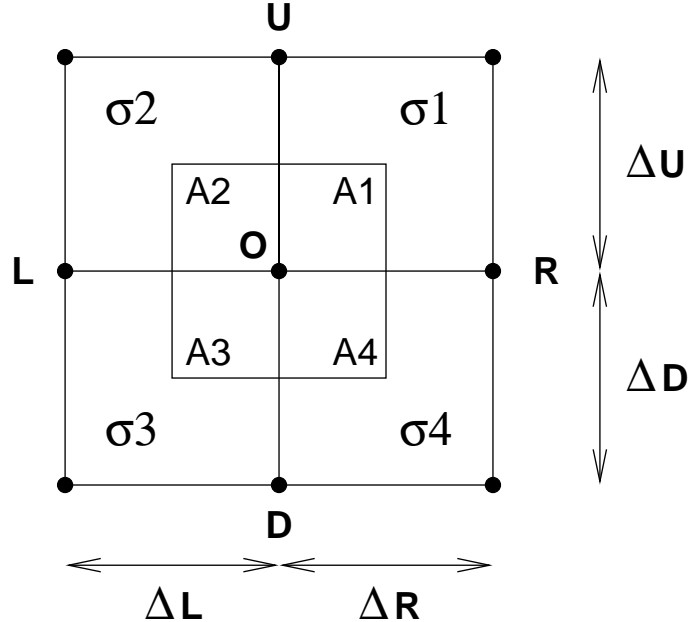


Figure A.1: Model node O and surrounding nodes of the rectangular mesh. The four sub-areas A_i with conductivities σ_i together compose an area A , reaching to the middle of the adjacent nodes (analog *Apra et al. [1997]*).

Solutions at the model boundary are not treated here. Application of the Gaussian theorem to the function ∇E_x for an area A as defined in Fig. A.1 and its surrounding line Γ at a node O yields :

$$\int_{A_O} (\nabla \cdot \nabla E_x) da = \int_{\Gamma_O} (\hat{\mathbf{n}} \cdot \nabla E_x) dl \quad (\text{A.3})$$

The right side of this equation can be approximated by first differences:

$$\begin{aligned} &\approx \left(\frac{\Delta_L + \Delta_R}{2} \right) \left[\frac{E_D - E_O}{\Delta_D} - \frac{E_O - E_U}{\Delta_U} \right] \\ &+ \left(\frac{\Delta_U + \Delta_D}{2} \right) \left[\frac{E_R - E_O}{\Delta_R} - \frac{E_O - E_L}{\Delta_L} \right] + \mathcal{O}(\Delta^2) \end{aligned} \quad (\text{A.4})$$

and the left side of equation A.3 (= integrated right side of eq. A.2) can be approximated as:

$$\begin{aligned} i\omega\mu_0 \int_A E_y(y, z) \sigma(y, z) dA &\approx i\omega\mu_0 E_O \int_A \sigma(y, z) dA \\ &\approx i\omega\mu_0 E_O \sum_{i=1}^4 \sigma_i A_i + \mathcal{O}(\Delta^3) \end{aligned} \quad (\text{A.5})$$

with the resistivities σ_i of the four adjacent rectangles of area A_i .

With $A = (\Delta_L + \Delta_R)(\Delta_U + \Delta_D)/4$, we finally have:

$$\begin{aligned} \frac{2}{\Delta_R + \Delta_L} \left[\frac{E_R - E_O}{\Delta_R} + \frac{E_L - E_O}{\Delta_L} \right] + \frac{2}{\Delta_U + \Delta_D} \left[\frac{E_D - E_O}{\Delta_D} + \frac{E_U - E_O}{\Delta_U} \right] \\ \approx -i\omega\mu_0 \tilde{\sigma}_O E_O \end{aligned} \quad (\text{A.6})$$

with $\tilde{\sigma}_O \equiv (1/A) \sum_{i=1}^4 \sigma_i A_i$.

The solution of this equation for the whole model is equivalent with the solution of a system of equations (again, the model boundary is disregarded)

$$\mathbf{K}\mathbf{v} = \mathbf{f} \quad (\text{A.7})$$

where \mathbf{v} is a vector consisting of the values for the electric field E_x at all model nodes, and \mathbf{f} is a vector of the same length containing boundary condition informations (*Rodi* [1976]). To bring equation A.6 into the desired form, it is reorganized in a way that $f_i = 0$ at all non-boundary nodes. The matrix \mathbf{K} is then symmetric and built up as follows:

$$\begin{bmatrix} \ddots & \ddots & 0 & \ddots & & 0 \\ \ddots & a_i & b_i & & c_i & \\ 0 & b_i & \ddots & \ddots & & \ddots \\ \ddots & & \ddots & \ddots & \ddots & 0 \\ & c_i & & \ddots & \ddots & \ddots \\ 0 & & \ddots & 0 & \ddots & \ddots \end{bmatrix} \begin{bmatrix} \vdots \\ \vdots \\ v_i \\ \vdots \\ \vdots \\ \vdots \\ v_M \end{bmatrix} = \begin{bmatrix} \vdots \\ 0 \\ \vdots \\ \vdots \\ \vdots \\ f_M \end{bmatrix} \quad (\text{A.8})$$

with the constants a_i , b_i , c_i resulting from equation A.6 divided by $4A = (\Delta_U + \Delta_D)(\Delta_L + \Delta_R)$

$$a_i = -2 \left(\frac{\Delta_{U_i} + \Delta_{D_i}}{\Delta_{R_i}} + \frac{\Delta_{U_i} + \Delta_{D_i}}{\Delta_{L_i}} + \frac{\Delta_{L_i} + \Delta_{R_i}}{\Delta_{D_i}} + \frac{\Delta_{L_i} + \Delta_{R_i}}{\Delta_{U_i}} \right) \quad (\text{A.9a})$$

$$+ i\omega\mu_0 (\sigma_{1i}\Delta_{R_i}\Delta_{U_i} + \sigma_{2i}\Delta_{L_i}\Delta_{U_i} + \sigma_{3i}\Delta_{L_i}\Delta_{D_i} + \sigma_{4i}\Delta_{R_i}\Delta_{D_i})$$

$$b_i = 2 \frac{\Delta_{L_i} + \Delta_{R_i}}{\Delta_{D_i}} \quad (\text{A.9b})$$

$$c_i = 2 \frac{\Delta_{U_i} + \Delta_{D_i}}{\Delta_{R_i}} \quad (\text{A.9c})$$

By inversion of equation A.7, the electric field is calculated at every model node, and the induction problem is solved.

A.2 Calculation of field components

Applying Maxwell equation A.10 on the horizontal electric field (still TE-mode), the magnetic field components can be derived:

$$\frac{\partial E_x}{\partial z} = i\omega B_y \quad (\text{A.10a})$$

$$\frac{\partial E_x}{\partial y} = -i\omega B_z \quad (\text{A.10b})$$

As the magnetic field is needed ‘only’ for the calculation of the synthetic data, these calculations are just performed for the field at the earth’s surface.

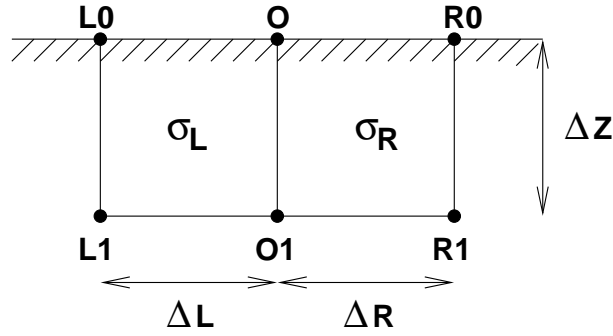


Figure A.2: A node O at the earth’s surface with adjacent nodes from the sides and below. The first layer of the earth is not the uppermost layer, as several air layers (~ 10) are following upwards (only for TE-mode).

- Calculation of B_y at the earth’s surface:

Approximation of the electric field by vertical and horizontal (right- and left-hand sided) Taylor-expansion yields (E stands for E_x in the following):

$$E_{O1} \approx E_O + \Delta_Z \frac{\partial E}{\partial z} \Big|_O + \frac{1}{2} \Delta_Z^2 \frac{\partial^2 E}{\partial z^2} \Big|_O + \mathcal{O}(\Delta^3) \quad (\text{A.11a})$$

$$\frac{\partial^2 E}{\partial y^2} \Big|_O \approx \frac{2}{\Delta_L \Delta_R} \left(\frac{\Delta_L E_{OR} + \Delta_R E_{OL}}{\Delta_L + \Delta_R} - E_O \right) + \mathcal{O}(\Delta^2) \quad (\text{A.11b})$$

Inserting the first of these equations into equation A.10a, we get:

$$B_{yO} \approx \frac{i}{\omega} \frac{1}{\Delta_Z} \left[E_{O1} - E_O - \frac{1}{2} \Delta_Z^2 \left(i\omega\mu_0\tilde{\sigma}_O E_O - \frac{\partial^2 E}{\partial y^2} \Big|_O \right) \right] \quad (\text{A.12})$$

with $\tilde{\sigma}_O = (\Delta_L\sigma_L + \Delta_R\sigma_R)/(\Delta_L + \Delta_R)$, and finally with equation A.11b:

$$B_{yO} \approx \frac{i}{\omega} \left[\frac{1}{\Delta_Z} E_{O1} + \frac{\Delta_Z}{\Delta_R(\Delta_L + \Delta_R)} E_{R0} + \frac{\Delta_Z}{\Delta_L(\Delta_L + \Delta_R)} E_{L0} - \left(i\frac{1}{2}\omega\mu_0\tilde{\sigma}_O\Delta_Z + \frac{1}{\Delta_Z} + \frac{\Delta_Z}{\Delta_L\Delta_R} \right) E_O \right] \quad (\text{A.13})$$

as is also derived in *Weaver* [1994], p. 185. In REBOCC, however, the calculation of the second vertical derivative of E , in spite of using equation A.2, is as follows:

$$\frac{\partial^2 E}{\partial z^2} \Big|_O \approx \frac{3}{4} \left(i\omega\mu_0\tilde{\sigma}_O E_O - \frac{\partial^2 E}{\partial y^2} \Big|_O \right) + \frac{1}{4} \left(i\omega\mu_0\tilde{\sigma}_O E_{O1} - \frac{\partial^2 E}{\partial y^2} \Big|_{O1} \right) \quad (\text{A.14})$$

Finally, following the equations from above, the horizontal magnetic field is approximated by calculating:

$$B_{yO} \approx a_O E_O + a_{L0} E_{L0} + a_{R0} E_{R0} + a_{O1} E_{O1} + a_{L1} E_{L1} + a_{R1} E_{R1}, \quad (\text{A.15})$$

with:

$$a_O = \frac{3}{8} \cdot \mu_0\tilde{\sigma}_O\Delta_Z - i \left(\frac{1}{\omega\Delta_Z} - \frac{3}{4} \frac{\Delta_Z}{\omega} \cdot \frac{1}{\Delta_L\Delta_R} \right) \quad (\text{A.16a})$$

$$a_{L0} = i \cdot \frac{3}{4\omega} \cdot \frac{\Delta_Z}{\Delta_L} \cdot \frac{1}{\Delta_L + \Delta_R} \quad (\text{A.16b})$$

$$a_{R0} = i \cdot \frac{3}{4\omega} \cdot \frac{\Delta_Z}{\Delta_R} \cdot \frac{1}{\Delta_L + \Delta_R} \quad (\text{A.16c})$$

$$a_{O1} = \frac{1}{8} \cdot \mu_0\tilde{\sigma}_O\Delta_Z - i \left(\frac{1}{\omega\Delta_Z} - \frac{1}{4} \frac{\Delta_Z}{\omega} \cdot \frac{1}{\Delta_L\Delta_R} \right) \quad (\text{A.16d})$$

$$a_{L1} = i \cdot \frac{1}{4\omega} \cdot \frac{\Delta_Z}{\Delta_L} \cdot \frac{1}{\Delta_L + \Delta_R} \quad (\text{A.16e})$$

$$a_{R1} = i \cdot \frac{1}{4\omega} \cdot \frac{\Delta_Z}{\Delta_R} \cdot \frac{1}{\Delta_L + \Delta_R}. \quad (\text{A.16f})$$

- Calculation of B_z :

The vertical magnetic field is approximated by calculating centered horizontal first differences:

$$B_{zO} \approx \frac{i}{\omega} \cdot \frac{1}{\Delta_R - \Delta_L} (E_{R0} - E_{L0}) + \mathcal{O}(\Delta^2). \quad (\text{A.17})$$

Apart from the electric field, the conductivities σ_L & σ_R of the adjacent model blocks have no influence in the calculation of the vertical magnetic field!

B Data and joint inversion responses

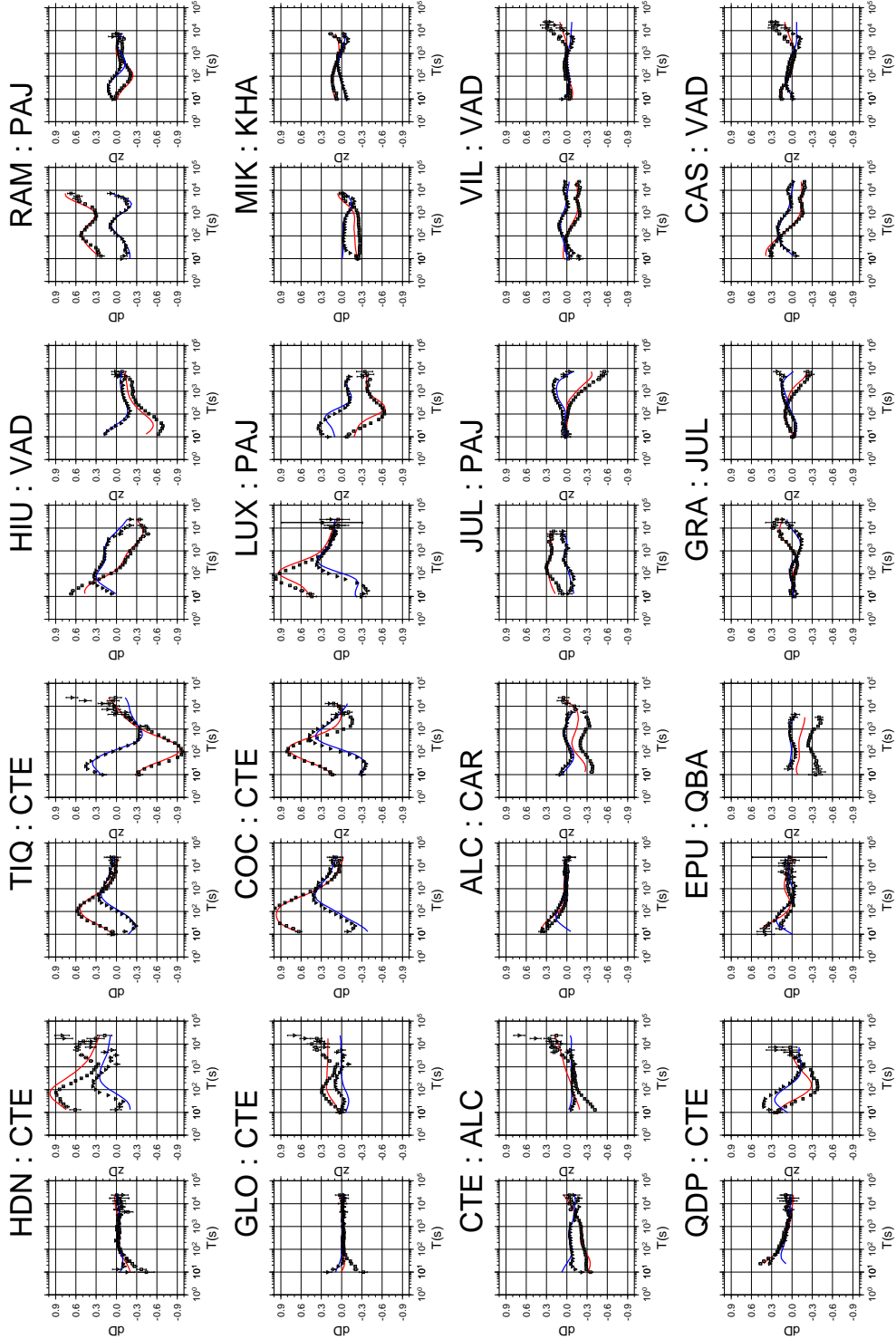


Figure B.1: Data fit for joint inversion of the inter-station geomagnetic transfer functions d_D (at each station left) and z_D (right) at representative sites from the ANCORP profile (SITE : REF. SITE). Red: real parts, blue: imaginary parts. West to east is from top left to bottom right, column by column. For model see figure 7.5 top.

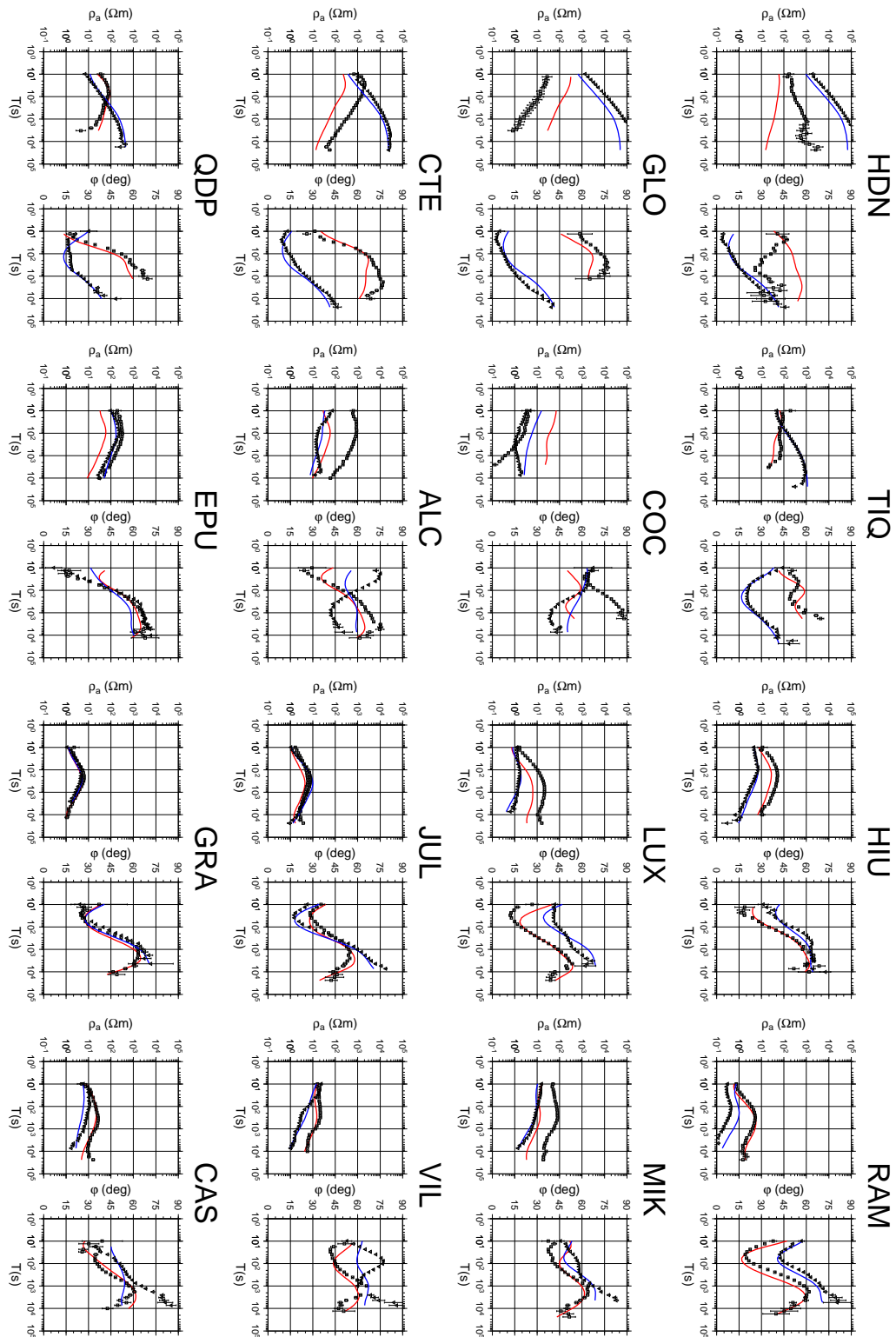


Figure B.2: Data fit for joint TE (red) and TM (blue) polarization impedance inversions at representative sites from the ANCORP profile. For model see figure 7.5 center.

B DATA AND JOINT INVERSION RESPONSES

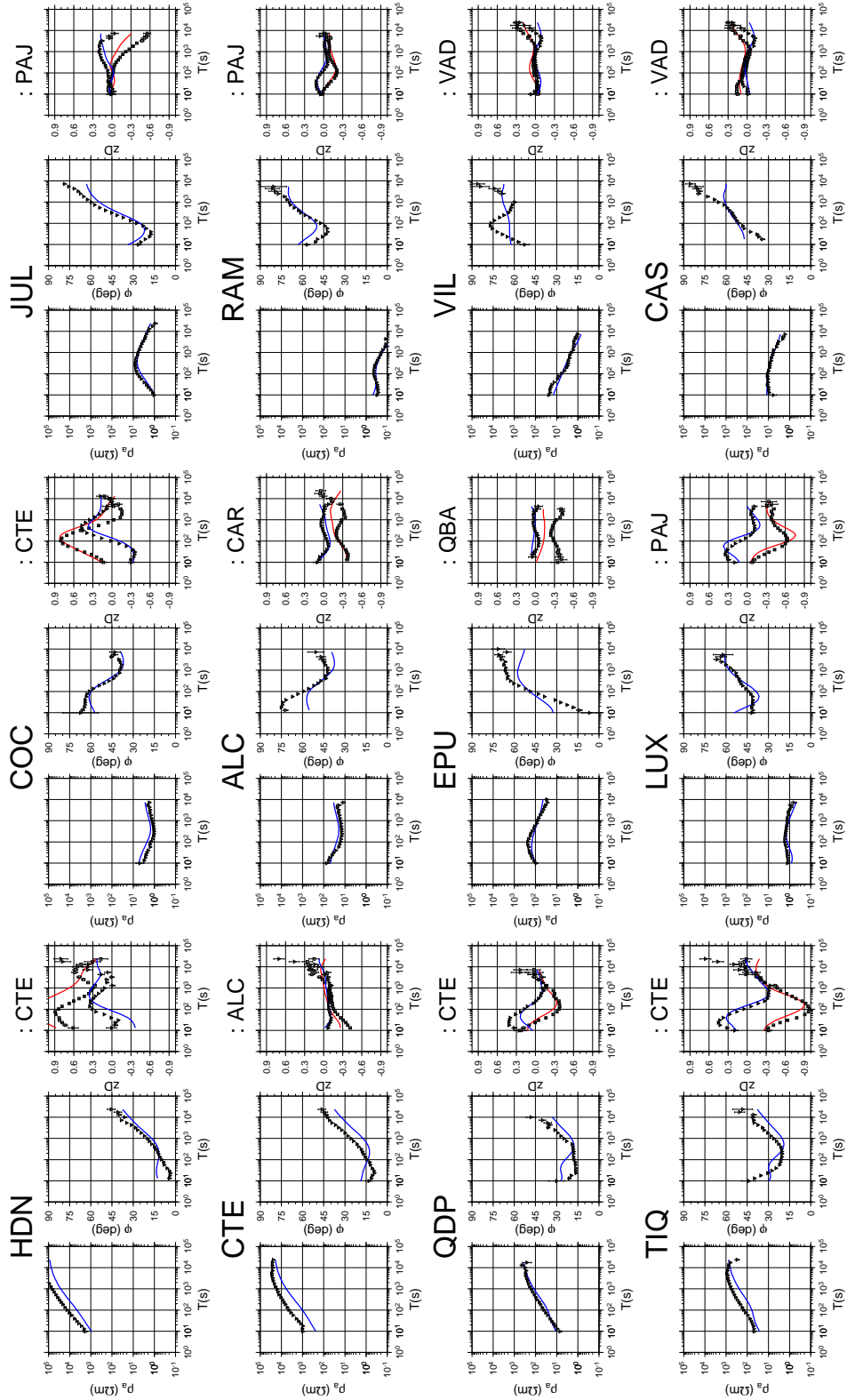


Figure B.3: Data fit for joint inversion of vertical to horizontal inter-station geomagnetic transfer functions z_D (right; : REF. SITE) and TM-polarization impedances at representative sites from the ANCORP profile. For model see figure 7.5 bottom.

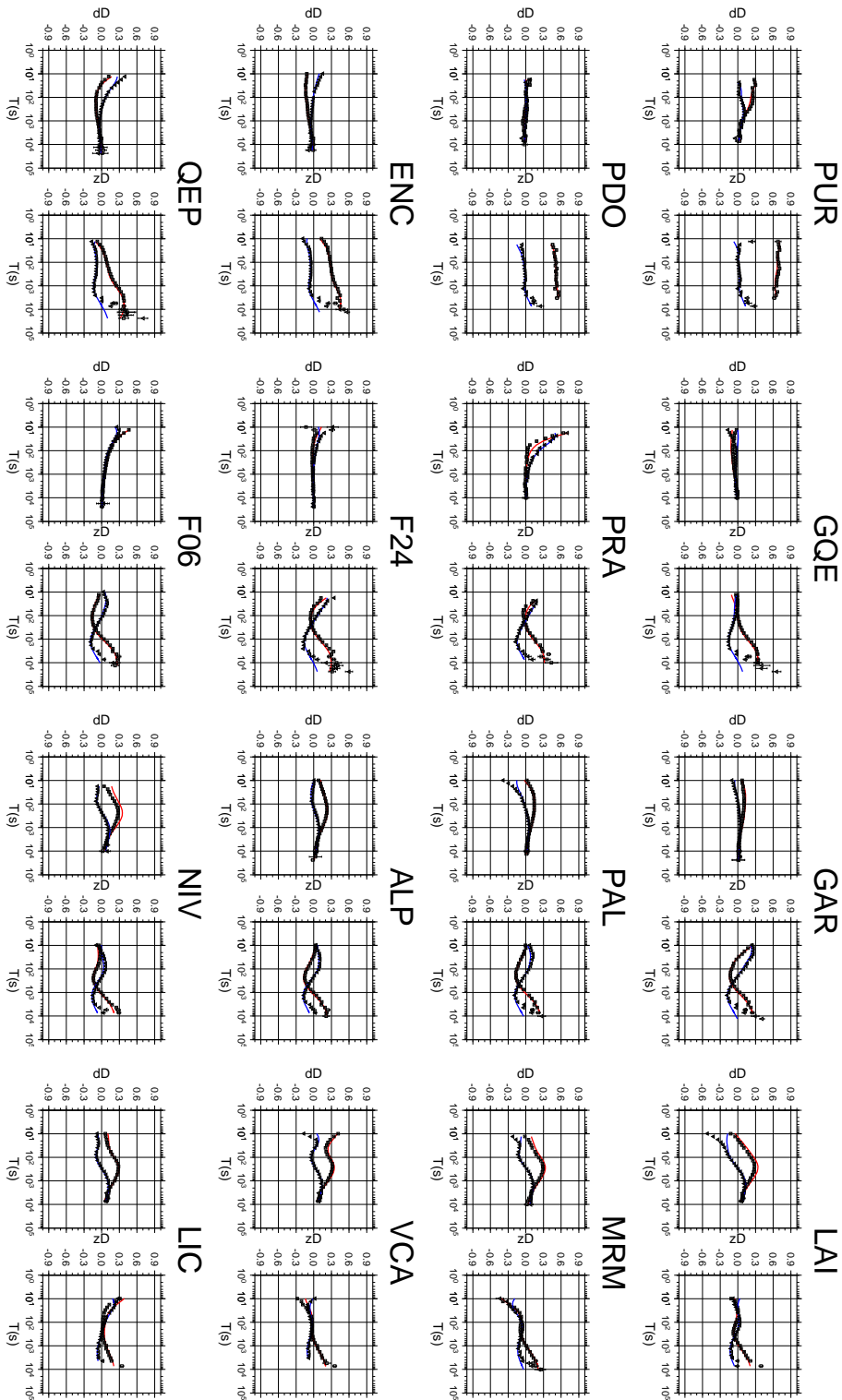


Figure B.4: Data fit for joint inversion of the inter-station geomagnetic transfer functions d_D (at each station left) and z_D (right) at representative sites from the northern profile of the south Chilean study area. Red: real parts, blue: imaginary parts. Reference site is CAN, located in the Central Valley. West to east is from top left to bottom right, column by column. For model see figure 7.11 top.

B DATA AND JOINT INVERSION RESPONSES

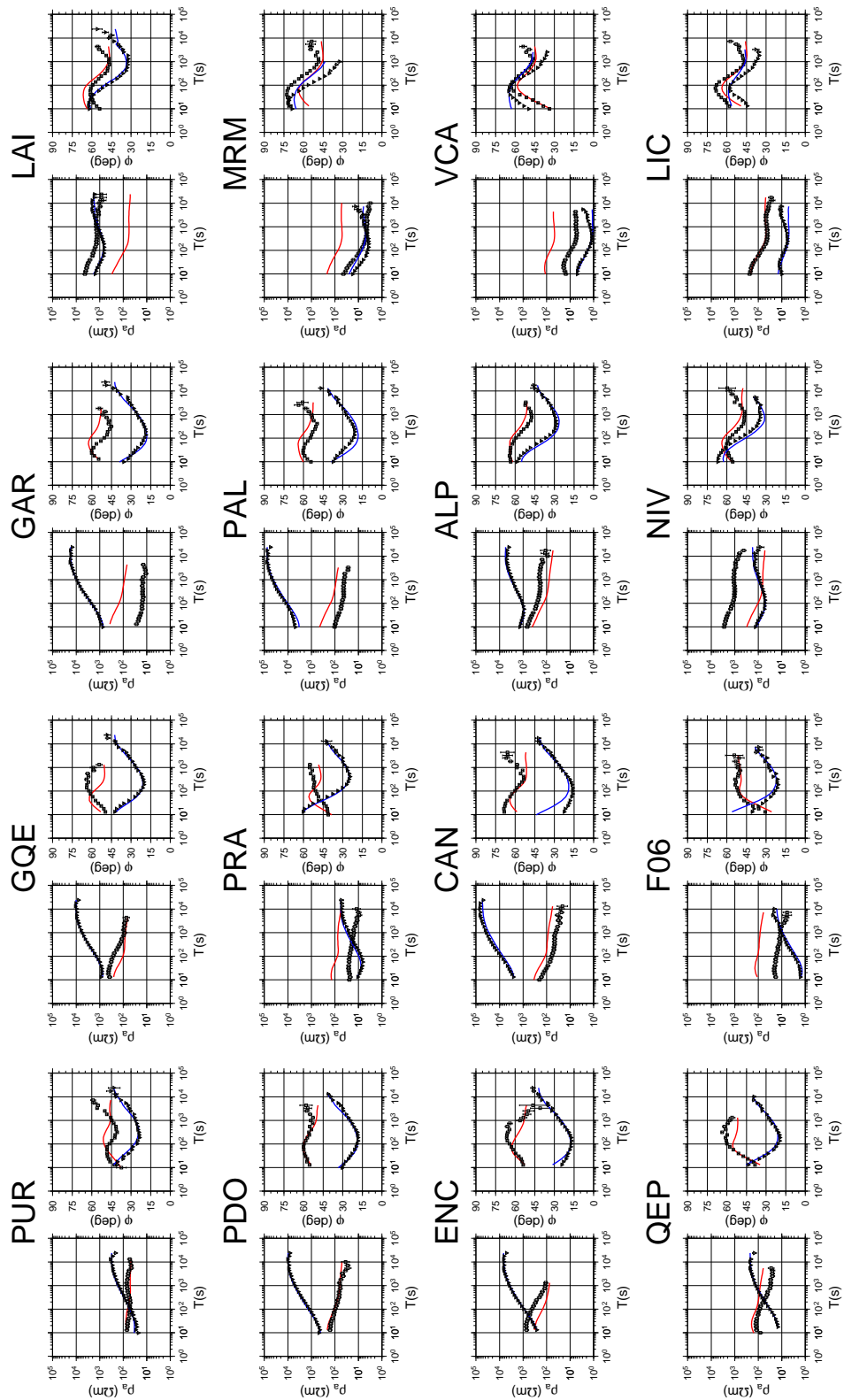


Figure B.5: Data fit for joint TE (red) and TM (blue) polarization impedance inversions at representative sites from the northern profile in southern Chile. For model see figure 7.11 center.

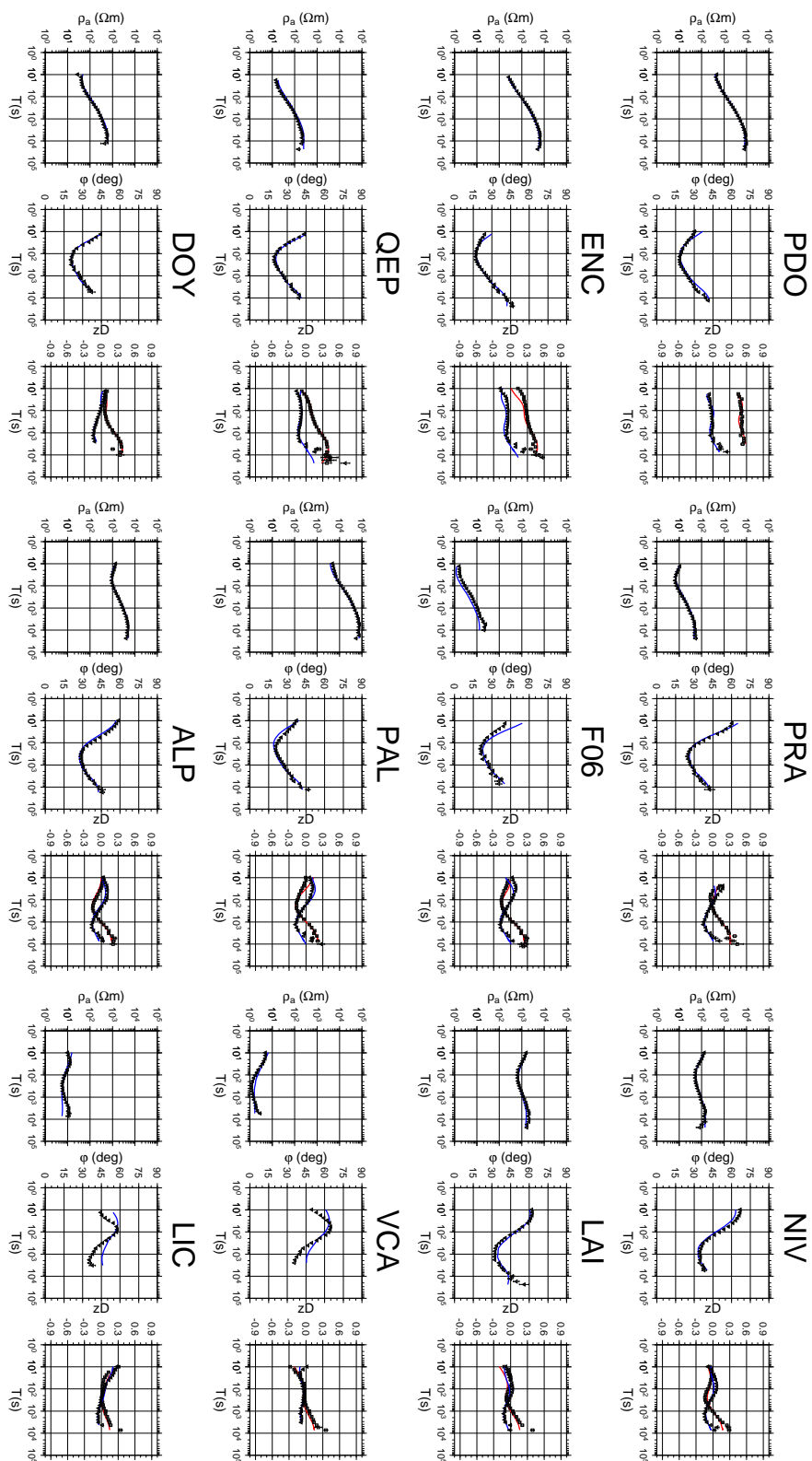


Figure B.6: Data fit for joint inversion of vertical to horizontal inter-station geomagnetic transfer functions z_D (right; reference: CAN) and TM-polarization impedances at representative sites from the northern profile in southern Chile. For model see figure 7.11 bottom.

C Station runtimes

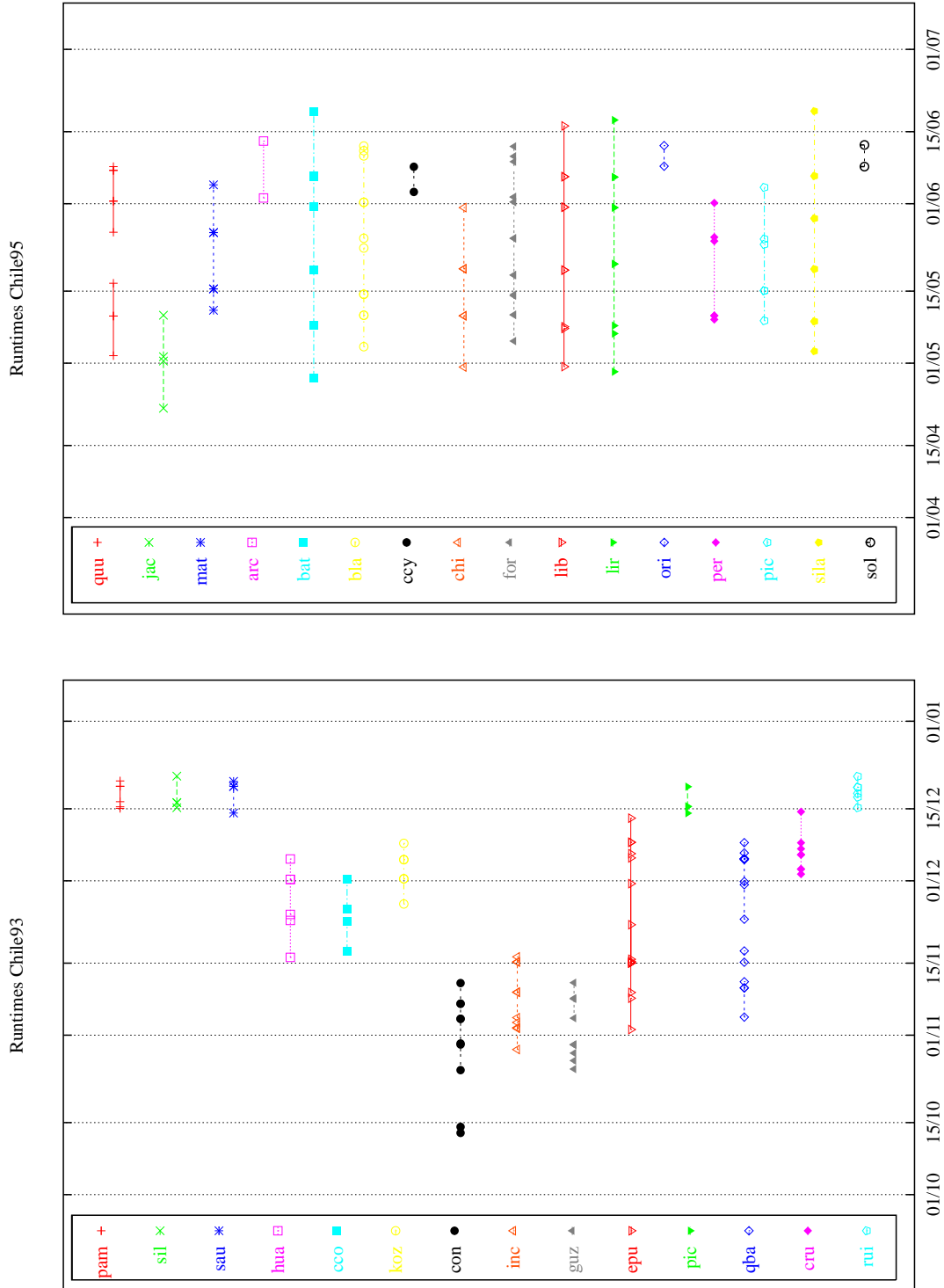


Figure C.1: Recording times from the north Chile campaigns in 1993 and 1995 (1993, just 5 field stations were deployed, 12 in 1995).

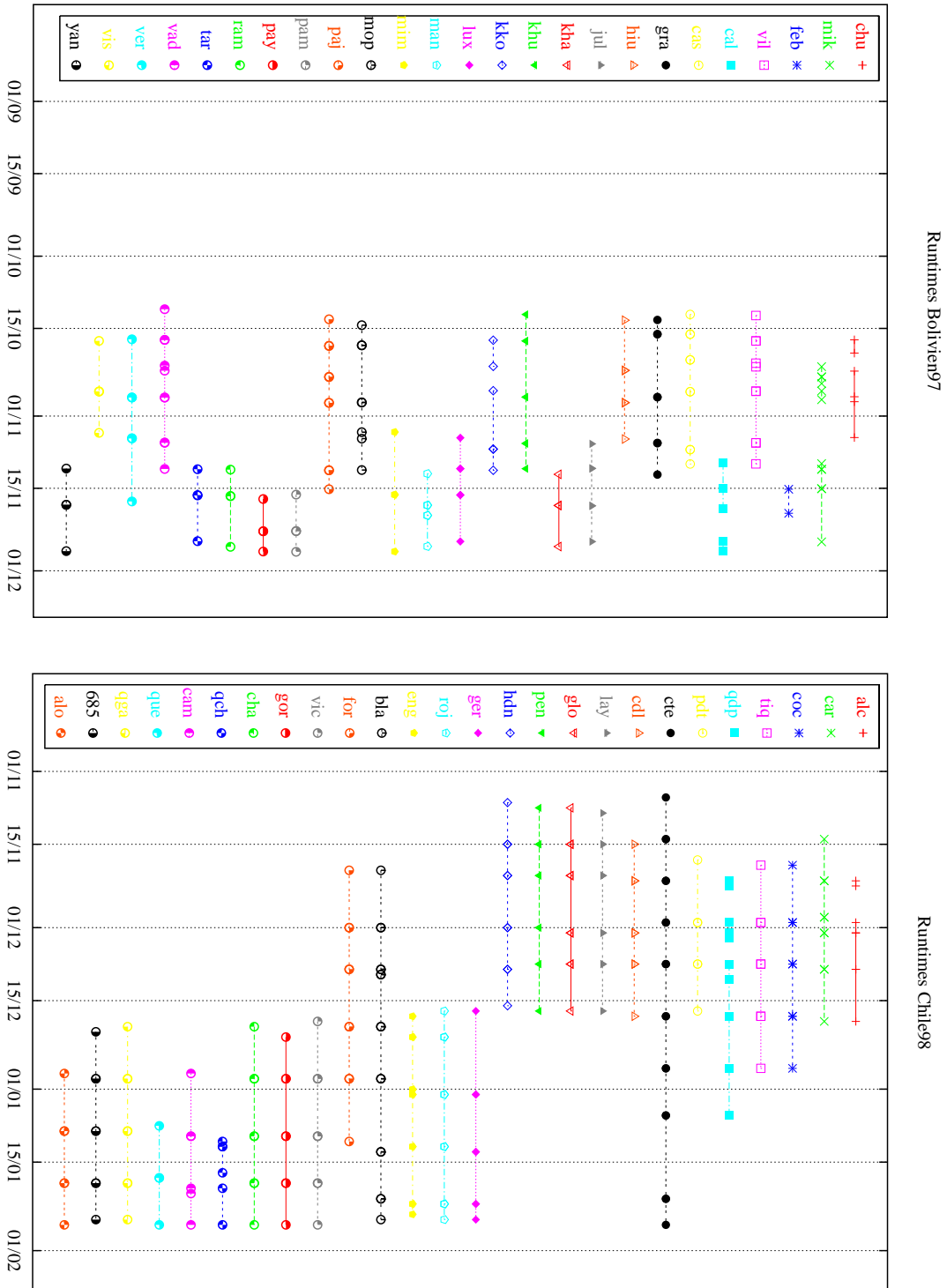


Figure C.2: Recording times from the SW Bolivia (1997) and N Chile (1998/99) campaigns (15 field stations deployed).

C STATION RUNTIMES

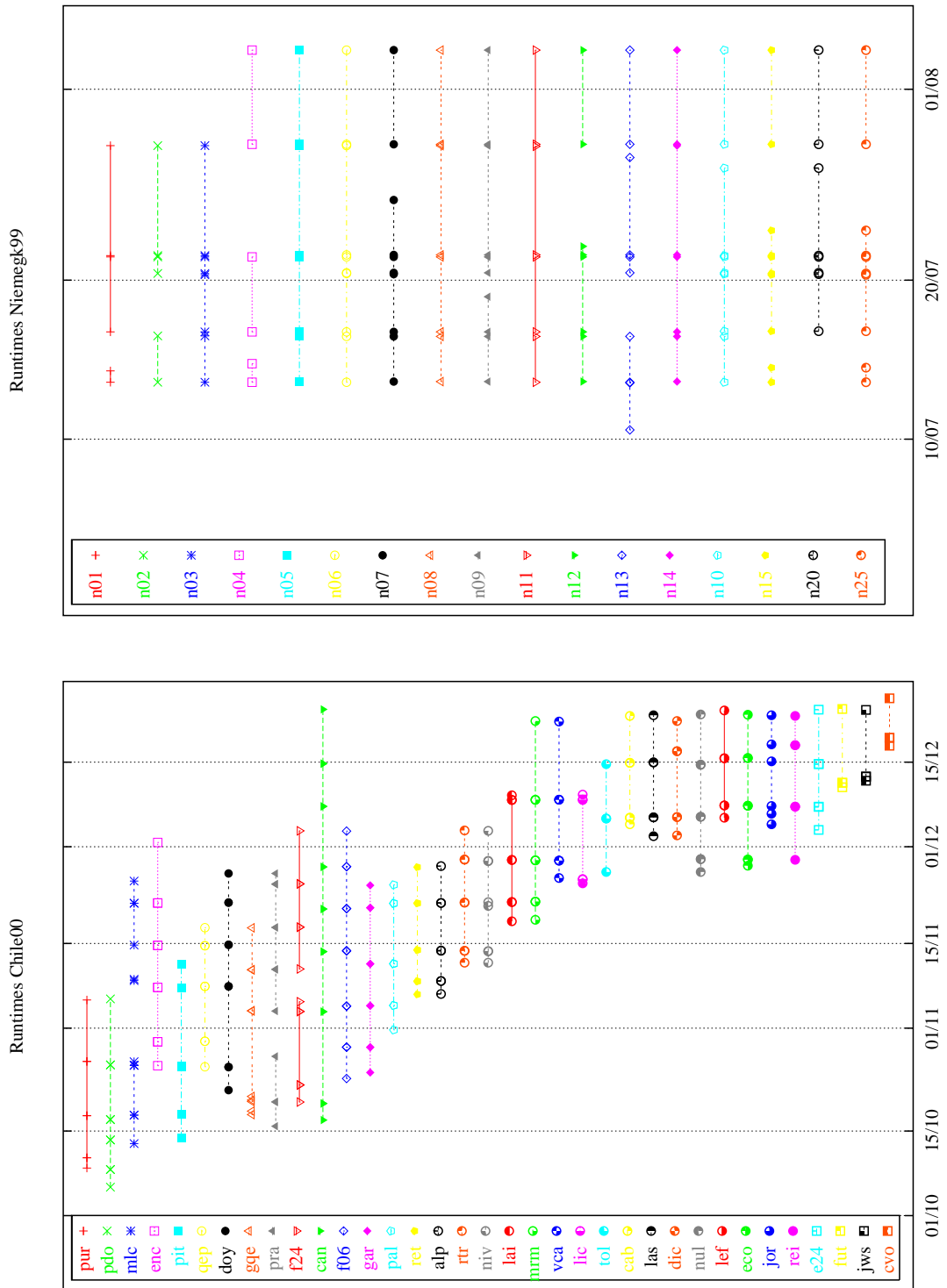


Figure C.3: Recording times from the south Chile campaign in 2000 and the calibration measurements in Niemeck 1999 (15 field stations, see appendix D).

D Analysis of an instrumental test recording

As all geomagnetic transfer functions discussed in this work are analyzed on a linear scale, the exact calibration of the instrument that measures the magnetic field is even more important for such an analysis than for an analysis of magnetotelluric transfer functions.

Individual calibrations for the fluxgate magnetometers (from MAGSON company) do not exist, and magnetic raw data from all stations of this thesis have been converted into magnetic variation data by applying exactly the same scaling factor and low pass filter corrections. To verify that the error originating from this equalization is tolerable, a three-week test recording was carried out in summer 1999 in the vicinity of the Niemegk observatory (state of Brandenburg), with all 16 available and in South America deployed equipments installed closely together and running simultaneously. Additionally, the potential differences between electrodes from two lines running in N-S and E-W direction, respectively, was recorded at all data loggers, their telluric amplifiers (constructed by E. Steveling, Göttingen) all connected in parallel to the same input. This part of the recording allowed the calculation of transfer functions between telluric amplifiers, which besides the amplification unit also bear a low pass with a cut-off frequency of ten seconds.

Data analysis has been performed using the bivariate and multivariate processing schemes described in section 4.1, and a simple univariate analysis without any robust features.

- Magnetometers

The robust local bivariate analysis calculating tipper vectors yields results that are optically merely distinguishable if displayed as induction arrows, and all tipper vectors look basically as the example given in figure D.1 (top). To display the differences between the results, the deviation of each station's transfer function from the over all instruments averaged value for the respective period are illustrated in histograms, shown in figure D.1 (bottom). These deviations amount to *orders of 0.01*, with a clear minimum in the period range of 100 s.

For the multivariate analysis, mostly five or six stations have been grouped for a joint processing, as this has also been done with the field data from the Andes. Here, we focus on the resulting horizontal transfer functions, namely $h_H + 1$ and $d_D + 1$ (notation as in 2.15). Figure D.2 shows results for one array, the first five stations related to the sixth station. Except for short periods, it is observed that the amplitudes of these quantities deviate from one by *less than 0.01*, and that the phase deviations approximate to *less than 0.5* towards longer periods.

The univariate processing without robust features was performed between equal geomagnetic channels of different stations. This analysis revealed a significant correlation between the global activity (deduced from Kp-Indices¹, which in three hour averages monitor the earth's magnetic field activity with respect to a mean daily variation) and the coherences between the processed channels. This correlation was observed for all magnetic components, but strongest for the vertical one (not illustrated). From these three types of data of analysis we can easily deduce a picture of the quality of our geomagnetic instruments. Though they are all installed closely together, robust techniques are generally affordable to deduce stable transfer func-

¹introduced by J. Bartels in 1949 in Göttingen, see *Menvielle and Berthelier* [1991]

D ANALYSIS OF AN INSTRUMENTAL TEST RECORDING

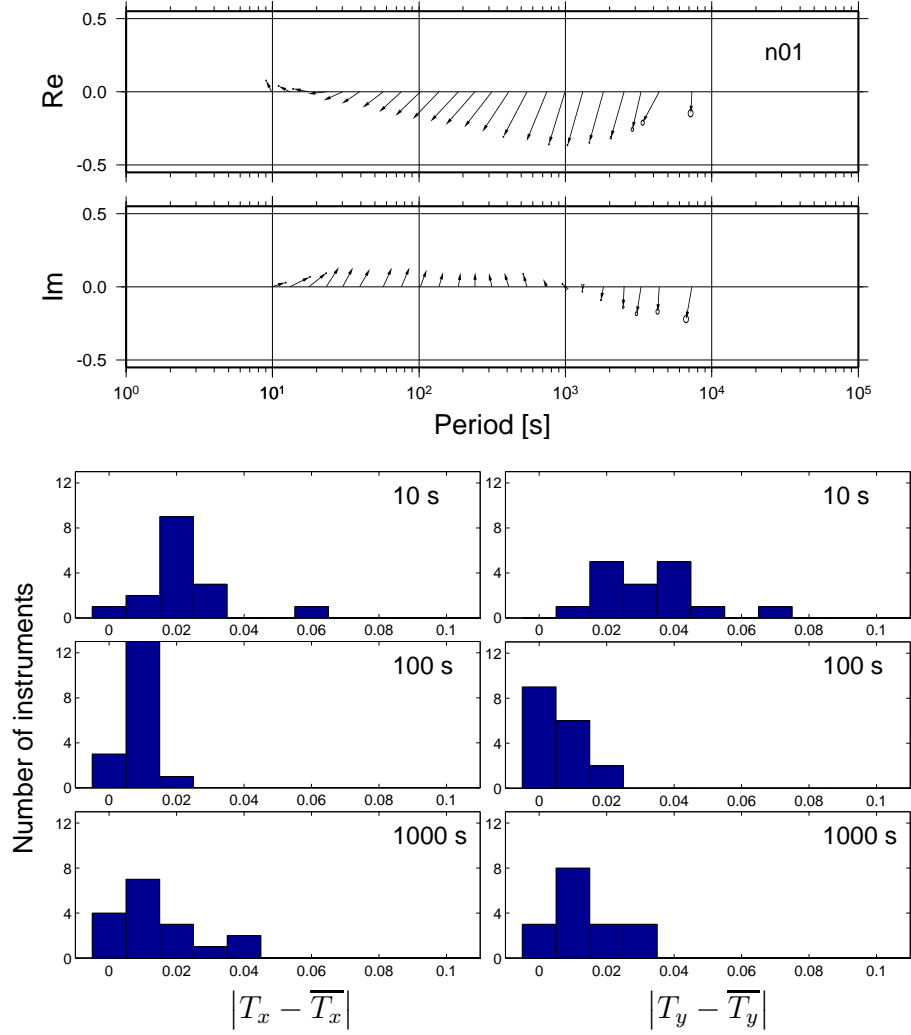


Figure D.1: Real and imaginary local induction vectors from one station (top) and histograms illustrating the transfer functions' deviation at all stations from the over all magnetometers averaged value (bottom, notation as in 2.14).

tions. For transfer functions involving the vertical component, which's natural field variation is of lower energy (i.e. induction vectors are 'shorter' than 1), the robust techniques are of higher relevance than for those between horizontal components. We can conclude that the fluxgate magnetometers all have significant instrumental noise in all channels (mainly for the period range between 10 s to 100 s), but apart from this they are calibrated well and, if the signal-to-noise ratio is high enough, do yield precise results:

$$\boxed{\text{SNR} > C_{\text{crit.}} \rightarrow |\Delta[\text{magn. transf. funct.}]| < 0.01}$$

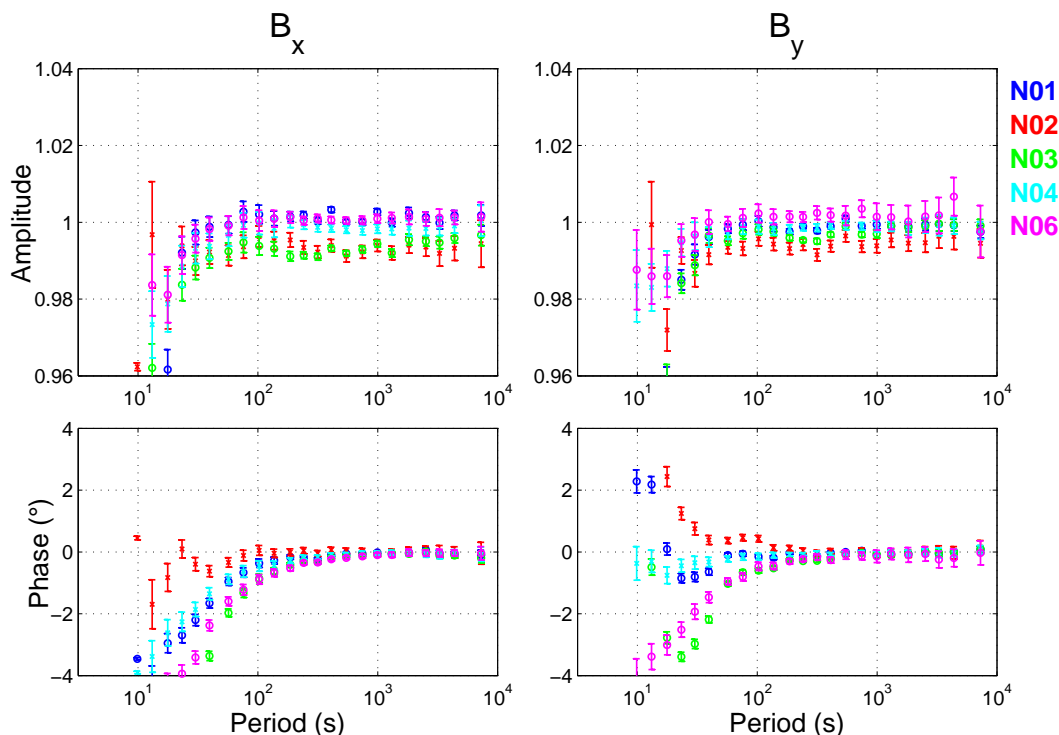


Figure D.2: Transfer functions from one multivariate processed array relating the horizontal components of five stations to the same component of the sixth station (left: $h_H + 1$; right: $d_D + 1$; notation as in 2.15). Note the small ranges at the ordinates.

- Telluric amplifiers

The telluric data have only been analyzed employing the non-robust univariate processing, calculating transfer functions between pairs of equal channels from different stations (figure D.3). The moduli of these transfer functions deviate just *some per mill* from one, which implies that with respect to the usual affordable accuracy in geo-electromagnetics, the preciseness of these instruments is by no means a matter of discussion.

However, another phenomenon is well illustrated by this analysis: the temporal drift of the data loggers' internal clock. This clock is synchronized just before each measurement with a connected GPS signal receiver, and at the end of the recording, the deviation between logger time and local time is again recorded. Such time deviations often amount to 100 ms per week of recording and more. In figure D.3, the two phase curves from any station–reference station combination have always the same trend. This circumstance explicitly identifies these curves as due to time drifts and makes clear that the phase deviations observed in the magnetic components in figure D.2 have the same reason.

Fourier theory tells us that time shifting of a signal by a constant t_0 is equivalent with the addition of $(2\pi/T) * t_0$ to the phase of the Fourier amplitude for period T . A transfer function between these two signals will thus have a phase curve proportional to $1/T$, as is approximately observed in figure D.3.

D ANALYSIS OF AN INSTRUMENTAL TEST RECORDING

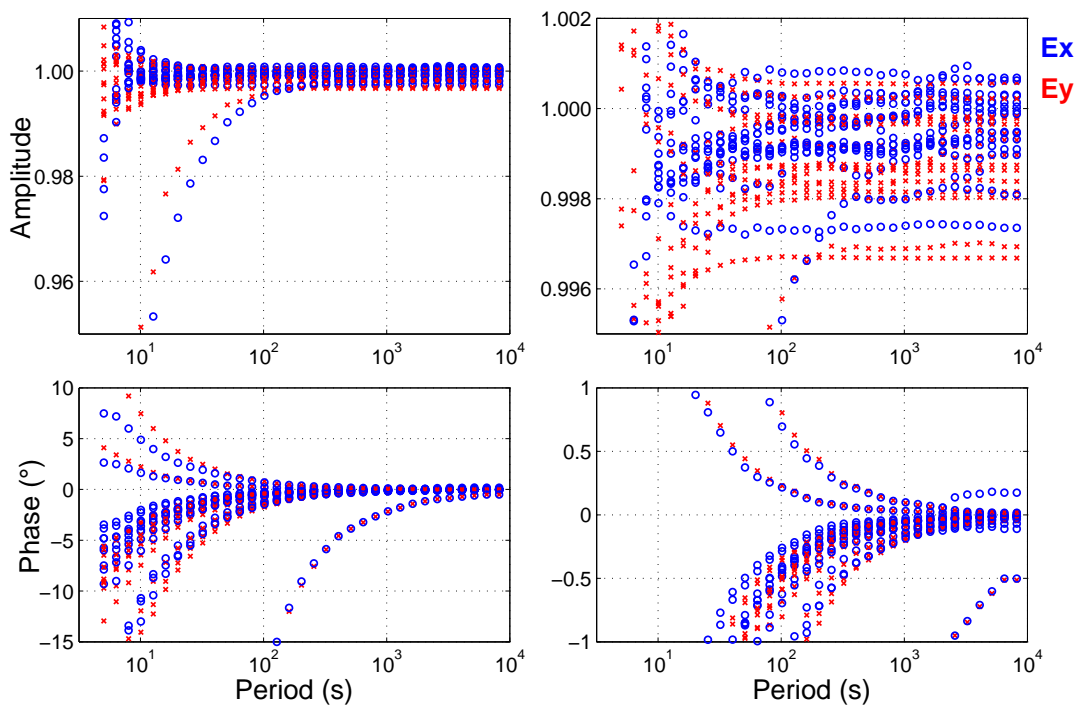


Figure D.3: Univariate transfer functions (no robust techniques) between equal electric components (N: blue and E: red) from different stations (references are varying). The right picture is just a zoom from the left one. One data-logger had severe timing errors. Again, note the small ranges at the ordinates.